



# SnO<sub>2</sub> nanoparticles confined in a graphene framework for advanced anode materials



Yun-Hwa Hwang<sup>a</sup>, Eun Gyoung Bae<sup>a</sup>, Kee-Sun Sohn<sup>b</sup>, Sangdeok Shim<sup>c,\*\*</sup>, Xiaokai Song<sup>d</sup>, Myoung Soo Lah<sup>d</sup>, Myoungho Pyo<sup>a,\*</sup>

<sup>a</sup> Department of Printed Electronics Engineering in WCU Program, Suncheon National University, Suncheon, Chonnam 540-742, Republic of Korea

<sup>b</sup> Faculty of Nanotechnology and Advanced Materials Engineering, Sejong University, Seoul 143-747, Republic of Korea

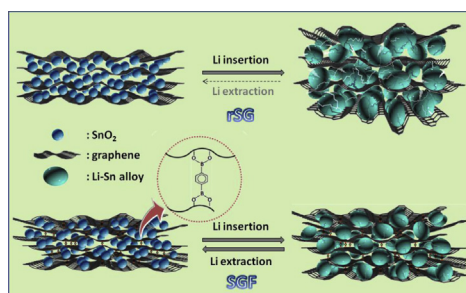
<sup>c</sup> Department of Chemistry & Pre-med, Suncheon National University, Suncheon, Chonnam 540-742, Republic of Korea

<sup>d</sup> Interdisciplinary School of Green Energy, Ulsan National Institute of Science & Technology, Ulsan-gun, Ulsan 689-798, Republic of Korea

## HIGHLIGHTS

- SnO<sub>2</sub> nanoparticles confined in a graphene framework is synthesized.
- The composite is utilized as anodes in Li ion batteries.
- SnO<sub>2</sub> particle aggregation is alleviated during charge–discharge cycles.
- Volume increase during Li alloying is also minimized in the composites.
- As a result, the composite shows excellent cyclability and rate capability.

## GRAPHICAL ABSTRACT



## ARTICLE INFO

### Article history:

Received 25 February 2013

Received in revised form

5 April 2013

Accepted 10 April 2013

Available online 21 May 2013

### Keywords:

Lithium ion batteries

Tin dioxide

Graphene

Framework

Anode

## ABSTRACT

SnO<sub>2</sub> nanoparticles (SNPs) entrapped in a graphene framework are synthesized for use as an anode material in Li ion batteries. A framework is prepared by covalently linking SNPs-anchored graphene oxide layers with diboronic acids. The framework provides the SNPs with more effective buffering than thermally reduced graphene oxide. SNPs in a graphene framework maintain the initial particle size and morphology after repeated charge–discharge cycles, with no inter-particle aggregation. The volume increase of the composite, accompanied by Li<sup>+</sup> insertion into SNPs, is also significantly suppressed. The isolation of an individual nanoparticle and the firmness of a framework, which are ascribed to densely cross-linked graphene layers, results in better cyclability and rate performance by comparison with thermally reduced SNPs-anchored graphene oxide.

© 2013 Elsevier B.V. All rights reserved.

## 1. Introduction

Tin dioxide (SnO<sub>2</sub>), which possesses a relatively high theoretical capacity (782 mAh g<sup>−1</sup>), is considered a promising alternative to a graphite anode (372 mAh g<sup>−1</sup>) for the development of next-generation lithium ion batteries with high energy densities [1]. SnO<sub>2</sub>, however, experiences a serious decay in reversible capacity during repeated charge–discharge (C–D) cycles, mainly due to the

\* Corresponding author. Tel.: +82 61 750 3638; fax: +82 61 750 5260.

\*\* Corresponding author.

E-mail addresses: [san90@suncheon.ac.kr](mailto:san90@suncheon.ac.kr) (S. Shim), [mho@suncheon.ac.kr](mailto:mho@suncheon.ac.kr) (M. Pyo).

irreversible large volume increase accompanied by lithium incorporation. Although amorphous  $\text{Li}_2\text{O}$  produced during the first few cycles can accommodate the volume strain to some extent, a dimensional expansion of as much as 260% eventually leads to an electrical disconnection that arises from the crumbling and pulverization of Sn domains [2].

One successful method is to relieve the mechanical stress by synthesizing  $\text{SnO}_2$  nanoparticles (SNPs) that have a regulated morphology. Nanospheres [3], nanowires [4,5], and hollow nanostructures such as nanotubes [6], nanospheres [7–10], and nanoboxes [11] fall into this category, and most possess better capacity retention than bulk  $\text{SnO}_2$  powders. However, commercial viability of the nanostructured  $\text{SnO}_2$  has been difficult because the critical grain size, below which pulverization of the SNPs is prevented, is far less than the unit cell size (thus, complete relief of the stress by decreasing the size is impossible) [12].

Another effective way to resolve the crumbling and pulverization of  $\text{SnO}_2$  during cycling is to create a hybrid of SNPs and carbonaceous materials [13–17], represented by graphene [18,19]. In SNPs/graphene nanocomposites, the ductility of graphene can buffer the substantial volume change of SNPs, while offering electrical conduction pathways to the composites. In addition, graphene composited in a well-controlled architecture prevents the re-aggregation of SNPs during C–D cycles [20,21], which can further help the cyclability of  $\text{SnO}_2$ . Besides these mechanical roles of graphene, the Li-storage capability of graphene itself [22–29] can make the SNPs/graphene composites possess a high specific capacity [30–39]. For example, Zhang et al. reported that SNPs, which were chemically anchored on both sides of a single layer graphene, retained a specific capacity of  $558 \text{ mAh g}^{-1}$  after 50 cycles at a current density of  $264 \text{ mA g}^{-1}$ , indicating a capacity

loss of 0.6% per C–D cycle [32]. Hydrothermally grown  $\text{SnO}_2$  nanorods on a graphene oxide support showed slightly better electrochemical performance. Xu et al. addressed that  $\text{SnO}_2$  nanorods-anchored graphene hybrids showed a capacity loss of 0.3% per cycle, retaining  $574 \text{ mAh g}^{-1}$  after 50 cycles at  $200 \text{ mA g}^{-1}$  [39]. Layer-by-layer structures consisting of alternating  $\text{SnO}_2$  and graphene layers were also investigated, in which the sandwiched architecture further improved the electrochemical stability of  $\text{SnO}_2$  [21,33].

Herein, we report that SNPs entrapped in a graphene framework (GF), in which the SNPs are free of inter-particle aggregation due to the isolation in the nanovoids of a GF (SGF) and the loss of electrical contact due to the suppression of volume change. This results in a relatively excellent cyclability (more than  $500 \text{ mAh g}^{-1}$  after 50 cycles at a rate of  $100 \text{ mA g}^{-1}$ ) and rate performance (ca.  $670 \text{ mAh g}^{-1}$  for 10th cycle at a rate of  $1.0 \text{ A g}^{-1}$ ), when compared with thermally reduced SNPs/graphene oxide (rSG). Fig. 1 shows the concept of this work, comparing the difference with rSG. The excellence of SGF can be ascribed to the covalently linked graphene layers, which provide the nanocomposite with the independence of an individual  $\text{SnO}_2$  nanoparticle (restriction of aggregation) and the firmness of a framework (restriction of excessive volume increase). We believe that the concept presented here is a versatile platform that is easily adaptable to other nanocomposite anode materials for lithium and/or sodium storage.

## 2. Experimental

Graphene oxide (GO) was synthesized by a modified Hummer's method [40] using artificial graphite (KS-6, TIMCAL). SNPs-anchored graphene oxide nanocomposite (SG) was synthesized

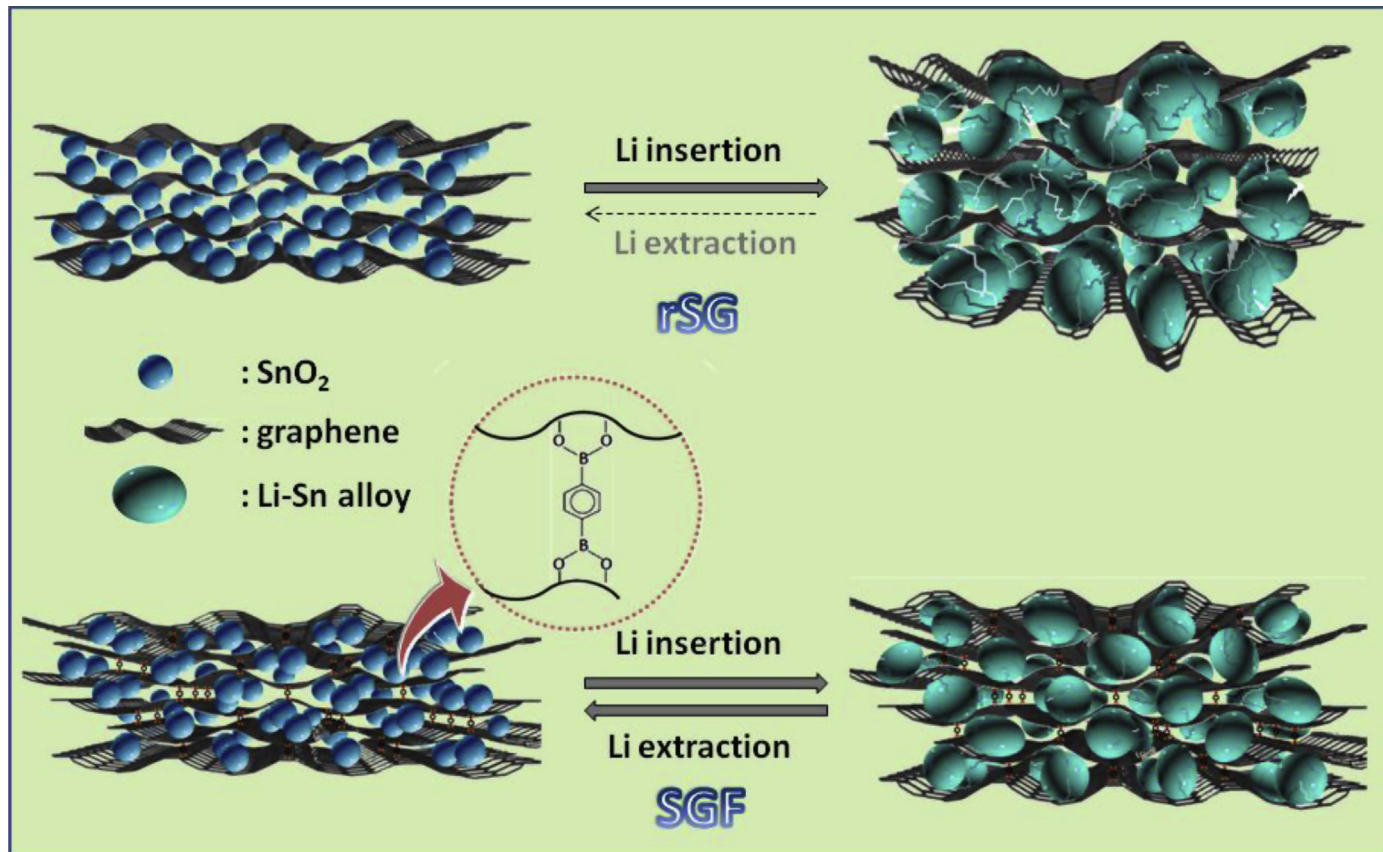


**Fig. 1.** Schematic diagram depicting the different behaviors between rSG and SGF during Li alloying/dealloying. When compared with rSG, the isolation of an individual  $\text{SnO}_2$  nanoparticle and the firmness of the GF that was provided by covalent bonding prevented particle aggregation and excessive volume change, respectively.

from GO and  $\text{Sn}^{2+}$  precursors, according to a previously reported procedure [37]. In a 100 mL mixture of DMSO and  $\text{H}_2\text{O}$  (the volume ratio of  $\text{DMSO}:\text{H}_2\text{O} = 9:1$ ), 100 mg of GO was dispersed by sonication for 1.5 h. To a stable GO solution, 1 g of  $\text{SnCl}_2 \cdot 2\text{H}_2\text{O}$  was added and was subsequently sonicated for 30 min. The mixture was refluxed at  $180^\circ\text{C}$  for 10 h to obtain a black suspension. The product was collected by centrifugation and then rinsed with anhydrous ethanol 6 times. Finally, the SG was dried at room temperature in air. For a comparative study, SG was annealed and reduced at  $400^\circ\text{C}$  for 2 h under an Ar atmosphere (rSG).

For the synthesis of the SGF, SG of 100 mg was dispersed in a 50 mL methanol solution containing 500 mg benzene-1,4-diboric acid (BDDBA) by sonication for 30 min, according to the procedure reported previously [41,42]. A small amount of GO (5 wt % with respect to oxidized SG) was added to assure a tightened framework. The cross-linking reaction was carried out in a Teflon-lined autoclave at  $85^\circ\text{C}$  for 48 h. The precipitate was collected and washed with methanol several times by centrifugation. The SGF was dried at room temperature in air without further treatment.

The changes in the stacking behavior of graphene and in the crystallinity of the SNPs were characterized by X-ray diffraction (XRD) using a Rigaku ULTIMA 4 equipped with  $\text{Cu K}_\alpha$  radiation at a scan rate of  $2^\circ \text{ min}^{-1}$ . Thermal gravimetric analysis (TGA, Q50, TA Instruments) was performed in air at  $10^\circ\text{C min}^{-1}$  to quantitatively compare oxygen functionalities. The change in the anode film thickness with Li alloying was examined using a JEOL JSM T-330A scanning electron microscope (SEM). The high-resolution transmission electron microscope (HRTEM) investigations were performed on a TEM JEOL 2100 instrument with an accelerating voltage of 200 kV. The samples were prepared by grinding and dispersing a powder in ethanol by ultrasonic treatment for 5 min. The suspensions were dropped onto standard holey carbon/Cu grids. The measurement of lattice fringe spacing recorded in HRTEM micrographs was made using a digital image analysis of the reciprocal space parameters. For a cross-sectional view, the SGF was embedded in an epoxy resin (Spurr, Electron Microscopy Sciences), followed by aging at  $70^\circ\text{C}$  for overnight. The sectioning was repeated to be the thickness of ca. 20 nm using an ultramicrotome (LEICA, Ultracut UCT). X-ray photoelectron spectroscopy (XPS) was carried out using a Thermo Fisher (K-Alpha) electron spectrometer with an Al  $\text{K}_\alpha$  X-ray source (excitation energy = 1486.6 eV).  $^{11}\text{B}$  magic angle spinning (MAS) nuclear magnetic resonance (NMR) spectrum was acquired at Bruker AVANCE II+ 400 MHz NMR system (KBSI Daegu Center). Raman spectra were recorded with a micro-Raman system (Alpha 300 s, WITec GmbH) using a 532 nm laser line with a 1- $\mu\text{m}$  beam diameter. To avoid a laser-induced heating effect, the laser power was controlled around 1 mW throughout the measurements.

The coin cells (CR 2032) of a Li/electrolyte/SGF (or rSG) configuration, in which the separator was sandwiched between 2 electrodes, were assembled in an Ar-filled glove box ( $\text{O}_2$ ,  $\text{H}_2\text{O} < 1\text{ ppm}$ ). The anode electrode was a mixture of 80% SGF (or rSG), 10% acetylene black (MTI, USA), and 10% poly(vinylidene fluoride). SGF-coated Cu foils were punched to form a disk with a diameter of 1.6 cm that was then welded to a stainless steel case. The separator was a Celgard 2400 microporous polypropylene membrane wetted in the electrolyte. The  $\text{LiPF}_6$  was dissolved in a mixture of ethylene carbonate and dimethylcarbonate (50:50 vol%) to a concentration of 1.0 M. A galvanostatic C–D cycle test was performed using an automatic WBCS 3000 battery cycler (WonA-Tech) in a potential range of 0.01–3.0 V vs.  $\text{Li}/\text{Li}^+$ . All assembled cells were stored for at least 1 h at room temperature before testing.

### 3. Results and discussion

#### 3.1. Synthesis of SGF nanocomposites

GO utilized for the preparation of SG possessed negligible graphitic domains. XRD showed no characteristic (002) diffraction of graphite at  $2\theta$  of  $26.5^\circ$  (see Fig. S1 in the Supplementary material). The oxygen functionality of GO was ca. 38% based on the weight loss at ca.  $200^\circ\text{C}$  in TGA (Fig. 2). The oxygen functionality was decreased to 3.2% (weight loss between 200 and  $300^\circ\text{C}$ ) for the SG. This implies that ca. half of the oxygen functional groups in GO were consumed during the formation of the SNPs (i.e., 3.2% with respect to 18.2% GO in SG means ca. 18% oxygen functionality remaining with respect to 100% GO). XRD patterns of the SG (see Fig. S1 in the Supplementary material) showed that an intense diffraction peak at  $2\theta$  of  $11.7^\circ$  in GO, corresponding to an inter-planar spacing ( $d$ -spacing) of 7.55 Å, almost completely disappeared after the anchoring of the SNPs. The absence of a long-range order is an indication that most GO sheets are present in the form of a single and/or a few layers after anchoring the SNPs.

To increase the crystallinity of  $\text{SnO}_2$ , SG powder was subjected to thermal treatment in air (2 h,  $400^\circ\text{C}$ ) [43] and subsequently reacted with a linker, BDDBA [41,42]. The XRD pattern of SGF (see Fig. S1 in the Supplementary material) shows the increase in crystallinity by thermal treatment. Comparison of the TGA curves of SGF with SG (Fig. 2) revealed a smaller oxygen functionality (weight loss in between 200 and  $300^\circ\text{C}$ ) and  $\text{SnO}_2$  content, due to the incorporation of BDDBA. Spectroscopy was also used to quantitatively determine the amount of BDDBA incorporated for SGF formation by measuring the concentration of unreacted BDDBA (see Fig. S2 in the Supplementary material). From a concentration of BDDBA that was unreacted with SG, the number of BDDBA moles involved in the framework formation was calculated to be  $2.9 \times 10^{-3}$  mol per g-GO, which was contrasted with the  $4.2 \times 10^{-3}$  mol per g-GO for a framework synthesized from  $\text{SnO}_2$ -free GO (GF), because of the reduction of available oxygen groups in the SG. It is noteworthy that the amounts of BDDBA involved in cross-linking (ca. 1 molecule of BDDBA per 23 C atoms for SGF vs. ca. 1 molecule of BDDBA per 12 C atoms for GF) appear to be proportional to the oxygen functionality. Note that ca. half of the oxygen groups of the GO remained in the SG, as explained above. This indicates that the presence of SNPs did not hamper the reaction between the oxygen groups of SG and BDDBA during the formation of SGF. The high BDDBA content in SGF implies the formation of a densely cross-linked framework, which can help the maintenance of the structural integrity of SNPs during C–D cycles.

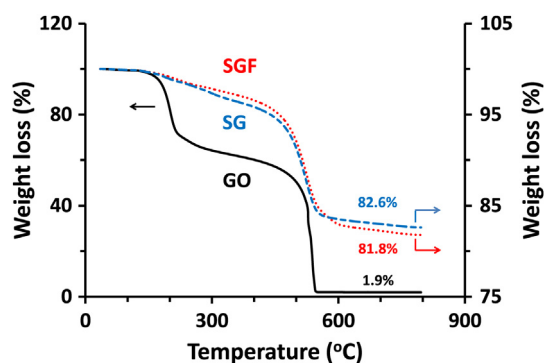
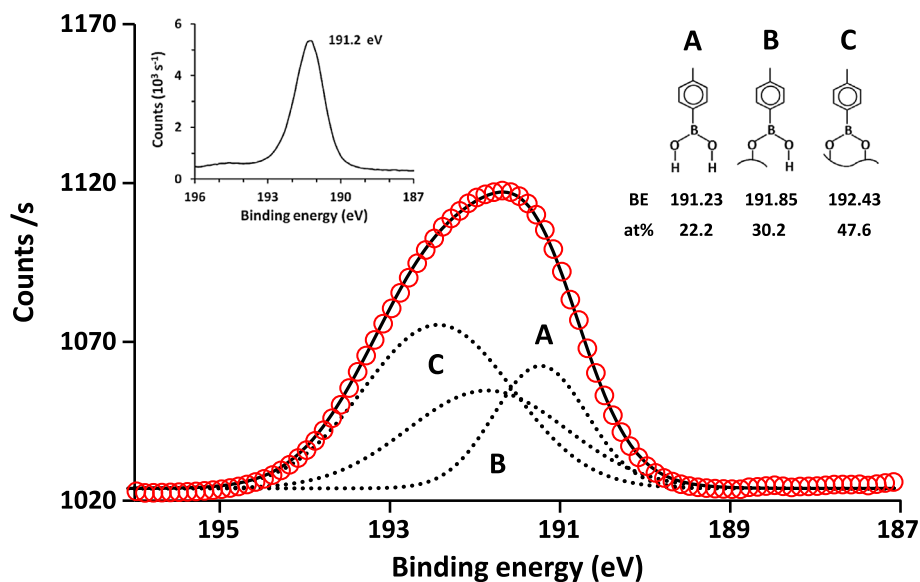


Fig. 2. TGA curves of GO, SG, and SGF obtained in air at  $10^\circ\text{C min}^{-1}$ .



**Fig. 3.** High-resolution XPS spectrum of B1s for SGF (red circles) with deconvoluted profiles (dotted lines) and sum of deconvoluted components (solid line). Insets show a spectrum of BDBA and possible chemical structures corresponding to deconvoluted peaks. (For interpretation of the references to colour in this figure legend, the reader is referred to the web version of this article.)

### 3.2. Characterization of SGF nanocomposites

The chemical nature of a boronic ester in SGF was examined by XPS. Fig. 3 shows a high-resolution XPS spectrum of boron and deconvoluted profiles. It was revealed that three different chemical states of boron (i.e., un-linked, mono-linked, and di-linked BDBA, denoted as A, B, and C in the inset, respectively.) existed. The integrated peak areas indicated that ca. 79% of BDBA (mono-linked and di-linked BDBA) contributed to the cross-linking. Solid-state  $^{11}\text{B}$  MAS NMR examination was also carried out to further confirm the chemical state of boron [44,45]. The spectrum shown in Fig. 4 revealed a similar quantification result of ca. 80% BDBA involved in cross-linking. Therefore, we believe that the XPS and NMR studies provided convincing evidence that most BDBA incorporated in SGF contributes to the framework formation.

The effect of cross-linking on the graphitic nature of graphene layers was also examined by Raman spectroscopy. Fig. 5 compares Raman spectra of GO, GF, and SGF in the first-order region ( $1100\text{--}1800\text{ cm}^{-1}$ ), showing characteristic peaks of carbonaceous materials at ca.  $1350\text{ cm}^{-1}$  (D band) and  $1592\text{ cm}^{-1}$  (G band) [40]. The disorder induced by the amorphization of graphite has been known to cause a characteristic band-broadening as well as an increase in the relative intensities of the D to G bands ( $I_D/I_G$ ), as a result of a reduction in the  $sp^2$  domain size [46]. In general, while highly ordered graphite has an  $I_D/I_G$  value of less than 0.3, the  $I_D/I_G$  value of highly disordered graphite falls between 1 and 2.6. The  $I_D/I_G$  values calculated for GO, GF, and SGF were 0.93, 1.00, and 1.65, respectively. In the case of GO, an  $I_D/I_G$  of 0.93 and an unsymmetrical shape for the G band agreed well with previous reports [46]. While the conversion of GO to GF resulted in a negligible change in the  $I_D/I_G$

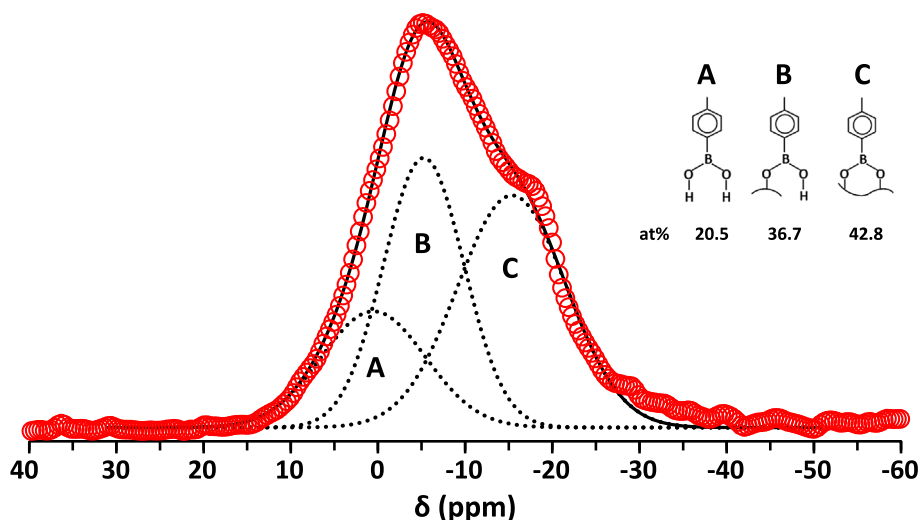


**Fig. 4.** Solid-state  $^{11}\text{B}$  MAS NMR spectrum of SGF (circles) with deconvoluted profiles (dotted lines) and sum of deconvoluted components (solid line). Inset shows possible chemical structures corresponding to deconvoluted peaks. Pulse sequence (one pulse), delay time (2 s), Larmor frequency (128.378 MHz), calibration ( $\text{H}_3\text{BO}_3$ ).



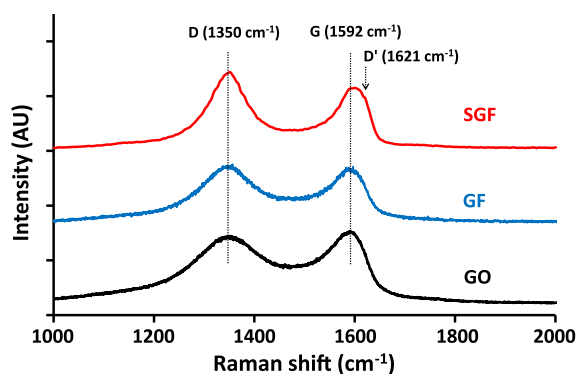


Fig. 5. Raman spectra of GO, GF, and SGF.

$I_G$ , the  $I_D/I_G$  of SGF was substantially increased, implying that the lattice vibration mode (the D band), which is Raman-inactive for the infinite graphene sheet, became active in a more conspicuous manner. The symmetry breaking is a likely reason, because the anchoring of the SNPs on GO and a subsequent tightening of SG via covalent bonds (cross-linking) made the graphene layers more wavy or curly, which reduced the  $sp^2$  domain size. A change in the shape of the G band from the GO to the SGF is also observable in Fig. 4. The asymmetry in GO is relieved in the SGF, showing a merged peak at  $1621\text{ cm}^{-1}$ . The D' band has been known to appear in graphite with a high concentration of defects due to phonon confinement [47]. Therefore, the appearance of the D' band and the resultant blue shift of the G band in SGF are also believed to be an indication of a substantial amount of distortion in the  $sp^2$  planarity, due to cross-linking. Note that neither a discernible peak shift, nor a D' band were seen in GF, implying that a covalent bond formation did not affect the  $sp^2$  planarity of the graphene layers in GF.

The HRTEM image of the SGF shown in the left panel of Fig. 6 indicates evenly distributed SNPs (3–5 nm in diameter) on the GO layers. The magnified view of  $\text{SnO}_2$  nanoparticles in the inset clearly shows the lattice fringes of  $\text{SnO}_2$ , revealing that the crystal structures of the SNPs were not affected by the cross-linking reaction. To investigate the relative distribution of SNPs and graphene layers, an ultramicrotomed cross-sectional view was investigated. The HRTEM image of a cross-section of SGF (middle panel of Fig. 6) shows SNPs isolated by graphene layers rather than interconnected to each other. No alternating layer-by-layer structures (i.e.,  $\text{SnO}_2$

layer and graphene layer) were observed, implying the possibility that SNPs were confined in nanovoids produced by GF. The thickness of the graphene layers was revealed to be ca. 2.2 nm, which corresponded to ca. 6 graphene layers. The electron diffraction pattern taken from the middle panel of Fig. 6 showed bright spots with characteristic diffraction rings from  $\text{SnO}_2$ . The right panel of Fig. 6 shows bright circular arcs from the aligned graphene stacks, which were overlapped with a (110) diffraction ring of SNPs. The appearance of graphene (002) diffraction arcs on top and bottom of an  $\text{SnO}_2$  (110) ring indicate that the graphene stacks constituting of a framework possesses a 1-dimensional directionality.

It should be mentioned that, although graphene layers were strongly bound to each other in the SGF, no noticeable difference in the Brunauer–Emmet–Teller (BET) surface area and pore volume were seen between SGF and rSG (see Fig. S3 in the Supplementary material). BET specific surface areas of  $190$  and  $200\text{ m}^2\text{ g}^{-1}$  and total pore volumes of  $0.154$  and  $0.153\text{ cm}^3\text{ g}^{-1}$  were obtained for SGF and for rSG, respectively. This suggests that the thermal treatment of SG can also produce a densely packed nanocomposite, comparable to SGF which was not thermally reduced.

### 3.3. Enhanced electrochemical performance of SGF

In order to confirm the effectiveness of a framework in SGF during the reversible Li alloy/dealloy with SNPs, we compared the capacity retention of SGF with that of rSG. The electrochemical performance of the rSG, prepared by the same procedure used in the present work, has reportedly already shown a mitigation of capacity fading during the first 20 cycles. A reversible capacity of  $690\text{ mAh g}^{-1}$  resulted in  $433\text{ mAh g}^{-1}$  after 20 C–D cycles at  $100\text{ mA g}^{-1}$  between  $0.005$  and  $1.5\text{ V}$  vs.  $\text{Li/Li}^+$ , which was indicative of ca. 37% capacity fading [37]. It should be pointed out that, although *in-situ* formed  $\text{Li}_2\text{O}$  and a buffering effect of graphene can improve capacity fading, the effectiveness relies on the weight fraction of  $\text{SnO}_2$ . In general, a higher  $\text{SnO}_2$  content results in worse capacity retention [48] since a stacked graphene structure in rSG is not durable enough to accommodate a large volume change and to prevent the aggregation of Sn domains, when  $\text{SnO}_2$  exists in a large fraction. Note that the rSG and the SGF examined in this study contained ca. 80 wt%  $\text{SnO}_2$ , which was substantially greater than the most other works [21,30–36,38,39]. Moreover, we cycled the rSG and the SGF between  $0.01$  and  $3.0\text{ V}$  in the present study, because the increase in the high-end cut-off potential usually causes more severe fading and, thus, the benefit of using a

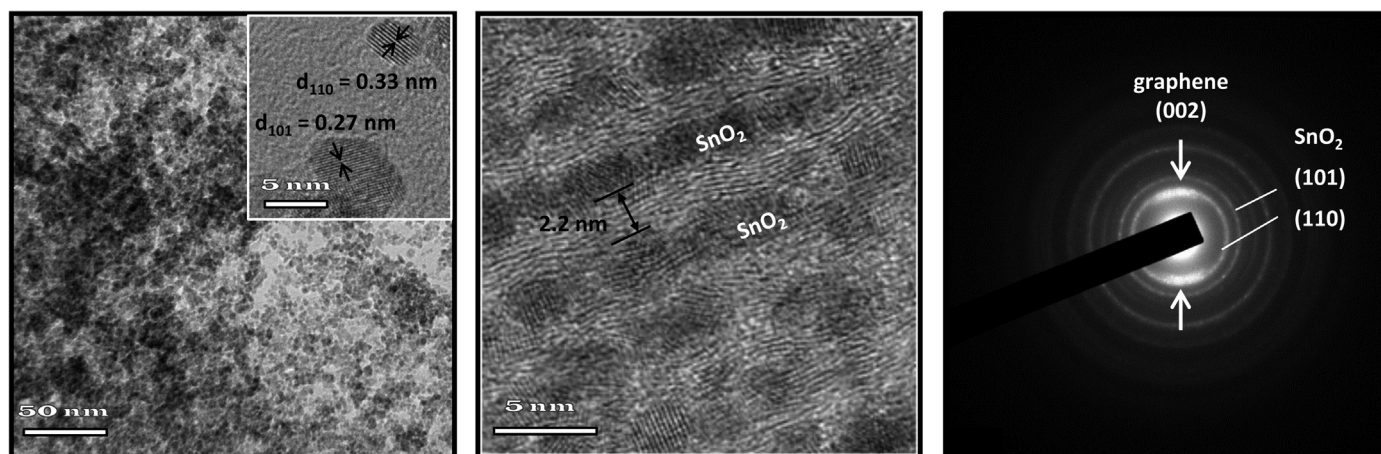


Fig. 6. [Left] HRTEM image of SGF (scale bar = 50 nm). The SGF was dispersed in ethanol by sonication and drop-casted on a holey carbon/Cu grid. Inset shows the lattice fringes of  $\text{SnO}_2$  (scale bar = 5 nm). [Middle] HRTEM image of the ultramicrotomed cross-section of SGF (scale bar = 5 nm). [Right] Electron diffraction pattern of SGF.

framework for the improvement of reversibility of  $\text{SnO}_2$  can be visualized more distinctly.

The  $dQ/dV$  curves of the first two cycles for SGF, obtained from C–D profiles scanned at  $100 \text{ mAh g}^{-1}$ , were demonstrated in Fig. 7A. It is evident that the charge was continuously accumulated during a discharge process from 3.0 V to 1.0 V, indicating the contribution of graphene layers to the total capacity. Besides the intercalation between graphene layers of graphitic domains [22–29] and the insertion into cavities [49] or into micropores [50], lithium can be stored in graphene nanosheets via a surface charge transfer process at a relatively high potential range [29,51]. The peak at 0.89 V during discharge was ascribed to the formation of solid–electrolyte interface layers and concurrent reduction of  $\text{SnO}_2$  to Sn and  $\text{Li}_2\text{O}$  (note that the peak height was substantially suppressed during the second scan). The peaks at 0.5 V and 0.2 V were believed due to a stepwise alloying process between lithium and Sn (of course, the reaction between graphene and lithium during this process cannot be completely neglected). During charging, two dominant peaks were observed at 0.5 V and 1.2 V. While the former indicates that the alloying process was reversible, the latter seems to imply a partially reversible formation of  $\text{SnO}_2$  from Sn and  $\text{Li}_2\text{O}$ . The plateau at 1.2 V during charging was also reported in previous works [35,36,38,39].

The panel B of Fig. 7 compares the capacity retention of rSG and SGF during 50 cycles. The higher specific capacities of both nanocomposites than the theoretical capacity of  $\text{SnO}_2$  ( $780 \text{ mAh g}^{-1}$ ) during the first few tens of cycles (10 cycles in rSG and 25 cycles in SGF) were believed due to a contribution from the surface charge transfer on graphene nanosheets, as explained above [29,51]. Fig. 7B indicates that the capacity fading of the rSG

was more pronounced, retaining only 12% of the reversible capacity ( $1291 \text{ mAh g}^{-1}$  of the second cycle was decreased to  $154 \text{ mAh g}^{-1}$  at the 50th cycle.). This was contrasted with the capacity fading of SGF, in which 41% of the reversible capacity ( $1282 \text{ mAh g}^{-1}$  of the second cycle) was retained. As a result, the similar initial reversible capacities of rSG and SGF ( $1291$  and  $1282 \text{ mAh g}^{-1}$ ) turned strikingly different after 50 cycles ( $154$  and  $521 \text{ mAh g}^{-1}$ ). At this point, it is worth mentioning that the thermal reduction of SGF resulted in the same capacity retention as that for rSG. Therefore, we believe that the superiority of SGF in capacity retention comes from the strong confinement of the SNPs between the graphene layers via BDBA linkers. The relatively weak attraction between graphene layers through the  $\pi$ – $\pi$  interaction in rSG is not sustainable during a rather extreme alloy/dealloy process.

The panels C and D of Fig. 7 show the 10th C–D curves of rSG and SGF at different current densities. When the current density was relatively low, both nanocomposites showed similar specific capacities (e.g.,  $1026$  and  $885 \text{ mAh g}^{-1}$  for rSG and  $1062$  and  $912 \text{ mAh g}^{-1}$  for SGF at  $0.1$  and  $0.3 \text{ A g}^{-1}$ , respectively). The difference, however, became conspicuous at high current densities. While the specific capacities of the rSG drastically decreased from  $701 \text{ mAh g}^{-1}$  at  $0.5 \text{ A g}^{-1}$  to  $182 \text{ mAh g}^{-1}$  at  $1.0 \text{ A g}^{-1}$ , the specific capacities of the SGF continuously decreased with current densities, leading to  $795, 674, 493$ , and  $334 \text{ mAh g}^{-1}$  at  $0.5, 1.0, 1.5$ , and  $2.0 \text{ A g}^{-1}$ , respectively. The improved rate capability of SGF is an additional benefit of using a framework. The retention of the substantial capacity of SGF at high current density can likely be ascribed to the alleviation of SNPs aggregation and crumbling which aggravate the charge transfer kinetics.

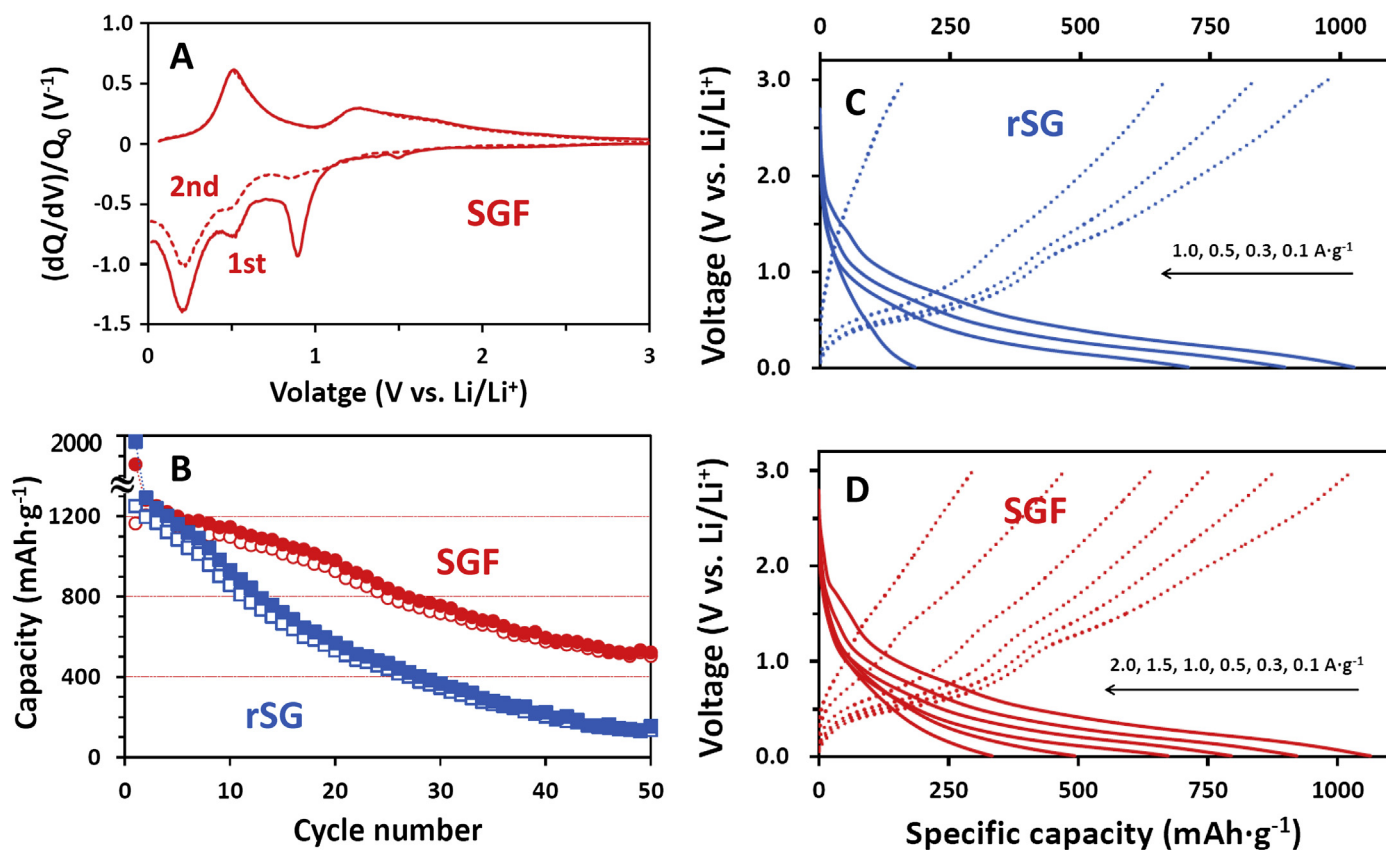
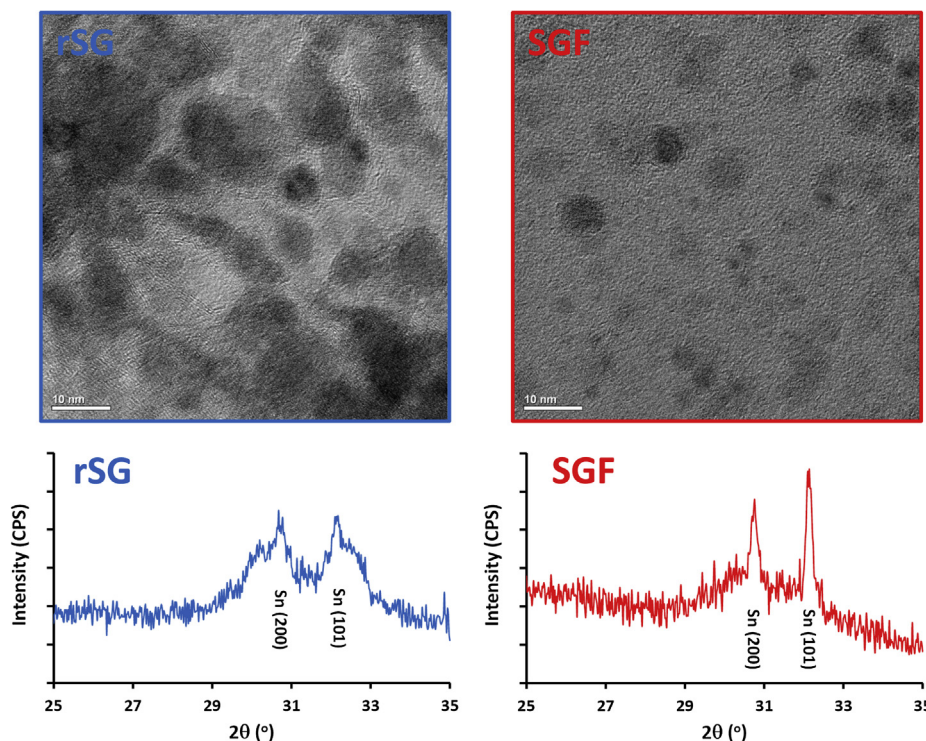


Fig. 7. [A] First and Second  $dQ/dV$  curves of SGF. [B] Charge (Li dealloying, open mark) and discharge (Li alloying, solid mark) capacity retention of rSG and SGF under a current density of  $100 \text{ mA g}^{-1}$  at  $20^\circ\text{C}$ . [C, D] Tenth C–D curves of rSG and SGF at various current densities. Specific capacity was normalized by the mass of active materials (graphene plus  $\text{SnO}_2$ ).



**Fig. 8.** HRTEM images and XRD patterns of rSG and SGF (scale bar = 10 nm). After 50 C–D cycles, coin cells were disassembled and anode materials were soaked in acetonitrile to remove remaining electrolytes. For HRTEM measurements, the powders were dispersed in ethanol by sonication and drop-casted on a holey carbon/Cu grid.

### 3.4. Suppressed SNP aggregation in SGF

After 50 C–D cycles, the changes in particle morphology for rSG and SGF were investigated. Fig. 8 compares the HRTEM images and the XRD patterns of rSG and SGF. It is evident that in the rSG, the SNPs were merged severely, losing the crystallinity of the metallic Sn. This implies that the improvement in the dimensional stability of the SNPs by  $\pi$ – $\pi$  stacked graphene layers was not satisfactory under the experimental conditions studied. The SGF, on the other hand, showed a quite different HRTEM image. No significant increase in particle size was observed, with the exception of a blurry contour due to electron density dilution by amorphous  $\text{Li}_2\text{O}$  [52]. The XRD image also indicated the maintenance of Sn crystallinity at a substantial fraction. This obvious distinction for SGF results from the isolation of individual  $\text{SnO}_2$  particles and, thus, in a hindrance of mergence.

### 3.5. Small volume change in SGF

To see the suppression of volume change by the framework formation in SGF, we compared the thickness changes for rSG and SGF during Li alloying. Li was alloyed by scanning the potential from the open circuit potential to 0.01 V (vs.  $\text{Li}/\text{Li}^+$ ), immediately after which the anodes were washed, dried, and cut using a doctor blade. Fig. 9 compares the cross-sectional SEM images of rSG and SGF. It is clear that, while the pristine anode films had the same thicknesses of ca. 7  $\mu\text{m}$  (inset), the volumes of the films increased with Li alloying, as expected. The extent of expansion, however, was noticeably different. In the rSG, the film thickness was increased to ca. 20  $\mu\text{m}$ , showing the disintegration of the composite due to a significant volume increase. In contrast, the volume increase was substantially suppressed in the SGF. The film thickness of Li-alloyed SGF was about half that of Li-alloyed rSG (ca. 11  $\mu\text{m}$ ). Because of the

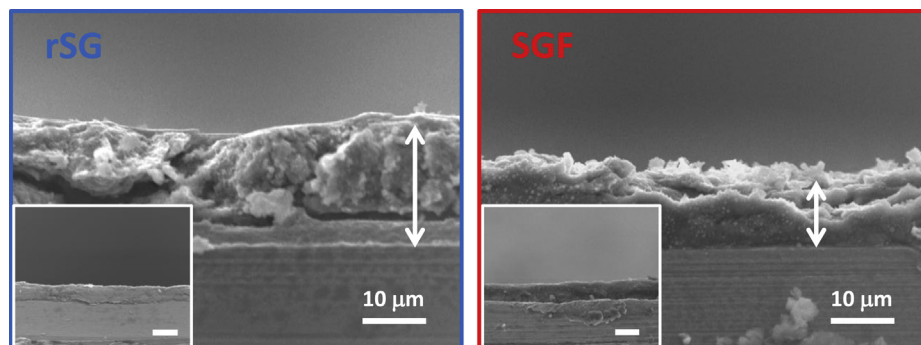


**Fig. 9.** Cross-sectional SEM images of Li-alloyed rSG and SGF at 0.01 V vs.  $\text{Li}/\text{Li}^+$ . Insets show cross-sectional SEM images of pristine rSG and SGF films (scale bar = 10  $\mu\text{m}$ ).



minimized volume increase, no distinct cracks were found. These contrasts between rSG and SGF indicate that the framework can function as a buffering material more effectively.

#### 4. Conclusions

A new type of SnO<sub>2</sub>/graphene nanocomposite is prepared, in which the SNPs are confined in a cross-linked graphene framework. Because graphene layers are linked by covalent bonds, the SNPs isolated in the nanovoids of the GF are freed from aggregation during the C–D cycling. The firmness of the GF also prohibits an excessive volume increase of the SNPs during Li alloying. The combination of the two effects of a framework provides the SGF with an improved capacity retention and rate performance, by comparison with rSG.

#### Acknowledgements

This research was supported by the WCU program through the Korea Science and Engineering Foundation funded by the Ministry of Education, Science and Technology (R31-10022).

#### Appendix A. Supplementary data

Supplementary data related to this article can be found at <http://dx.doi.org/10.1016/j.jpowsour.2013.04.159>.

#### References

- [1] M. Winter, J.O. Besenhard, *Electrochim. Acta* 45 (1999) 31–50.
- [2] W.-J. Zhang, *J. Power Sources* 196 (2011) 13–24.
- [3] Z.P. Guo, G.D. Du, Y. Nuli, M.F. Hassan, H.K. Liu, *J. Mater. Chem.* 19 (2009) 3253–3257.
- [4] Z. Ying, Q. Wan, H. Cao, Z.T. Song, S.L. Feng, *Appl. Phys. Lett.* 87 (2005) 1,131,081–1,131,083.
- [5] M.-S. Park, G.-X. Wang, Y.-M. Kang, D. Wexler, S.-X. Dou, H.-K. Liu, *Angew. Chem. Int. Ed.* 46 (2007) 750–753.
- [6] Y. Wang, J.Y. Lee, H.C. Zeng, *Chem. Mater.* 17 (2005) 3899–3903.
- [7] D. Deng, J.Y. Lee, *Chem. Mater.* 20 (2008) 1841–1846.
- [8] X.W. Lou, Y. Wang, C. Yuan, J.Y. Lee, L.A. Archer, *Adv. Mater.* 18 (2006) 2325–2329.
- [9] Y. Wang, F. Su, J.Y. Lee, X.S. Zhao, *Chem. Mater.* 18 (2006) 1347–1353.
- [10] S. Ding, J.S. Chen, G. Qi, X. Duan, Z. Wang, E.P. Giannelis, L.A. Archer, X.W. Lou, *J. Am. Chem. Soc.* 133 (2011) 21–23.
- [11] Z. Wang, D. Luan, F.Y.C. Boey, X.W. Lou, *J. Am. Chem. Soc.* 133 (2011) 4738–4741.
- [12] J. Wolfenstine, *J. Power Sources* 79 (1999) 111–113.
- [13] Y. Li, S. Zhu, Q. Liu, J. Gu, Z. Guo, Z. Chen, C. Feng, D. Zhang, W.-J. Moon, *J. Mater. Chem.* 22 (2012) 2766–2773.
- [14] Y. Wang, H.C. Zeng, J.Y. Lee, *Adv. Mater.* 18 (2006) 645–649.
- [15] S. Guo, S. Dong, *Chem. Soc. Rev.* 40 (2011) 2644–2672.
- [16] J.G. Zhou, H.T. Fang, J.M. Maley, J.Y.P. Ko, M. Murphy, Y. Chu, R. Samyinaiken, T.K. Sham, *J. Phys. Chem. C* 113 (2009) 6114–6117.
- [17] J. Zhou, J. Wang, H. Fang, T.-K. Sham, *J. Mater. Chem.* 21 (2011) 5944–5949.
- [18] X. Li, X. Meng, J. Liu, D. Geng, Y. Zhang, M.N. Banis, Y. Li, J. Yang, R. Li, X. Sun, M. Cai, M.W. Verbrugge, *Adv. Funct. Mater.* 22 (2012) 1647–1654.
- [19] D. Wang, X. Li, J. Wang, J. Yang, D. Geng, R. Li, M. Cai, T.-K. Sham, X. Sun, *J. Phys. Chem. C* 116 (2012) 22149–22156.
- [20] Z.-S. Wu, G. Zhou, L.-C. Yin, W. Ren, F. Li, H.-M. Cheng, *Nano Energy* 1 (2012) 107–131.
- [21] X. Wang, X. Cao, L. Bourgeois, H. Guan, S. Chen, Y. Zhong, D.-M. Tang, H. Li, T. Zhai, L. Li, Y. Bando, D. Golberg, *Adv. Funct. Mater.* 22 (2012) 2682–2690.
- [22] P. Guo, H. Song, X. Chen, *Electrochem. Commun.* 11 (2009) 1320–1324.
- [23] Z.-S. Wu, W. Ren, L. Xu, F. Li, H.-M. Cheng, *ACS Nano* 5 (2011) 5463–5471.
- [24] E. Yoo, J. Kim, E. Hosono, H.-S. Zhou, T. Kudo, I. Honma, *Nano Lett.* 8 (2008) 2277–2282.
- [25] D. Pan, S. Wang, B. Zhao, M. Wu, H. Zhang, Y. Wang, Z. Jiao, *Chem. Mater.* 21 (2009) 3136–3142.
- [26] J.S. Park, S.M. Cho, W.-J. Kim, J. Park, P.J. Yoo, *ACS Appl. Mater. Interf.* 3 (2011) 360–368.
- [27] X. Li, D. Geng, Y. Zhang, X. Meng, R. Li, X. Sun, *Electrochem. Commun.* 13 (2011) 822–825.
- [28] Y. Liu, J.S. Xue, T. Zheng, J.R. Dahn, *Carbon* 34 (1996) 193–200.
- [29] I. Mochida, C.-H. Ku, Y. Korai, *Carbon* 39 (2001) 399–410.
- [30] J. Yao, X. Shen, B. Wang, H. Liu, G. Wang, *Electrochem. Commun.* 11 (2009) 1849–1852.
- [31] S.-M. Paek, E. Yoo, I. Honma, *Nano Lett.* 9 (2009) 72–75.
- [32] L.-S. Zhang, L.-Y. Jiang, H.-J. Yan, W.D. Wang, W. Wang, W.-G. Song, Y.-G. Guo, L.-J. Wan, *J. Mater. Chem.* 20 (2010) 5462–5467.
- [33] D. Wang, R. Kou, D. Choi, Z. Yang, Z. Nie, J. Li, L.V. Saraf, D. Hu, J. Zhang, G.L. Graff, J. Liu, M.A. Pope, I.A. Aksay, *ACS Nano* 3 (2010) 1587–1595.
- [34] H. Kim, S.-W. Kim, Y.-U. Park, H. Gwon, D.-H. Seo, Y. Kim, K. Kang, *Nano Res.* 3 (2010) 813–821.
- [35] P. Lian, X. Zhu, S. Liang, Z. Li, W. Yang, H. Wang, *Electrochim. Acta* 56 (2011) 4532–4539.
- [36] S. Ding, D. Luan, F.Y.C. Boey, J.S. Chen, X.W. Lou, *Chem. Commun.* 47 (2011) 7155–7157.
- [37] J. Liang, W. Wei, D. Zhong, Q. Yang, L. Li, L. Guo, *ACS Appl. Mater. Interf.* 4 (2012) 454–459.
- [38] J. Xie, S.-Y. Liu, X.-F. Chen, Y.-X. Zheng, W.-T. Song, G.-S. Cao, T.-J. Zhu, X.-B. Zhao, *Int. J. Electrochem. Sci.* 6 (2011) 5539–5549.
- [39] C. Xu, J. Sun, L. Gao, *J. Mater. Chem.* 22 (2012) 975–979.
- [40] H. Kim, D.-H. Seo, S.-W. Kim, J. Kim, K. Kang, *Carbon* 49 (2012) 326–332.
- [41] J. Burres, S. Gadipelli, J. Ford, J.M. Simmons, W. Zhou, T. Yildirim, *Angew. Chem. Int. Ed.* 49 (2010) 8902–8904.
- [42] G. Srinivas, J.W. Burres, J. Ford, T. Yildirim, *J. Mater. Chem.* 21 (2011) 11323–11329.
- [43] T.P. Kumar, A.M. Stephan, P. Thayananth, V. Subramanian, S. Gopukumar, N.G. Renganathan, M. Raghavan, N. Muniyandi, *J. Power Sources* 97, 98 (2001) 118–121.
- [44] J.W.E. Weiss, D.L. Bryce, *J. Phys. Chem. A* 114 (2010) 5119–5131.
- [45] M. Bishop, N. Shahid, J. Yang, A.R. Barron, *Dalton Trans.* 17 (2004) 2621–2634.
- [46] K.N. Kudin, B. Ozbas, H.C. Schniepp, R.K. Prud'homme, I.A. Aksay, R. Car, *Nano Lett.* 8 (2008) 36–41.
- [47] T. Livneh, T.L. Haslett, M. Moskovits, *Phys. Rev. B* 66 (2002) 1,951,101–19,151,011.
- [48] Y. Li, X. Lv, J. Lu, J. Li, *J. Phys. Chem. C* 114 (2010) 21,770–21,774.
- [49] A. Mabuchi, K. Tokumitsu, H. Fujimoto, T. Kasuh, *J. Electrochem. Soc.* 142 (1995) 1041–1046.
- [50] Y. Wu, C. Jiang, C. Wan, E. Tsuchida, *Electrochem. Commun.* 2 (2000) 272–275.
- [51] J.R. Dahn, T. Zheng, Y. Liu, J.S. Xue, *Science* 270 (1995) 590–594.
- [52] C.-M. Wang, W. Xu, J. Liu, J.-G. Zhang, L.V. Saraf, B.W. Arey, D. Choi, Z.-G. Yang, J. Xiao, S. Thevuthasan, D.R. Baer, *Nano Lett.* 11 (2011) 1874–1880.